Proceedings of ASME Turbo Expo 2026
Turbomachinery Technical Conference and Exposition
GT2026
June 15-19, 2026, Milan, Italy

GT2026-174893

EVALUATION OF PARTICLE DEGRADATION OF A YTTERBIUM DISILICATE GAS TURBINE COATING IN A COMBUSTION ENVIRONMENT

Jamesa L. Stokes **Michael J. Presby**
NASA Glenn Research Center
Cleveland, OH

ABSTRACT

Ytterbium disilicate ($Yb_2Si_2O_7$) is a state-of-the-art topcoat material used in environmental barrier coatings (EBCs) to protect SiC-SiC composites from water vapor induced corrosion in gas turbine engines. However, its degradation by thermochemical and thermomechanical particle interactions may limit its use in next generation engine systems. $Yb_2Si_2O_7$ is susceptible to recession due to solid particle erosion. Similarly, ingested particles in the engine can become molten and thermochemically corrode $Yb_2Si_2O_7$ by dissolution and reprecipitation. Several static furnace tests have been performed on $Yb_2Si_2O_7$ to elucidate methods of degradation, although dynamic testing in an engine-relevant environment has not been carried out. Ultimately, testing and evaluation of materials that incorporates all environmental damage modes will allow for an accurate assessment of long-term durability and operating lifetime. This work details the investigation of particle-induced erosion and corrosion of $Yb_2Si_2O_7$ in NASA Glenn's Erosion Burner Rig Facility. Coating durability was investigated as a function of test temperature, particle size, and deposition rate. Thermal cycling was also incorporated into testing to determine the interplay of heating/cooling cycles with particle degradation. Overall, these analyses will be used to determine coating robustness in an engine relevant environment, which will contribute to greater understanding in the design of future coating systems.

Keywords: EBC; CMAS; erosion; high temperature; $Yb_2Si_2O_7$; burner rig

1. INTRODUCTION

The implementation of silicon carbide (SiC)-based ceramic matrix composites (CMCs) in the hot section of gas turbines [1] has been enabled by the development of environmental barrier coatings (EBCs) to protect components from water vapor induced corrosion in the harsh engine environment. By reducing oxidation and preventing the recession of SiC-based CMCs, their lighter weight as well as higher temperature capability over traditional nickel-based superalloys will result in greater fuel efficiency for next generation engine systems. Prevailing state-of-the-art (SOA) EBCs typically utilize ytterbium disilicate ($Yb_2Si_2O_7$) as a topcoat material, as it has comparable thermal expansion behavior to SiC-based CMCs and suitable water vapor volatility resistance [2,3]. The harsh engine environment, however, introduces a host of additional concerns for EBC material selection and design. These can include degradation due to foreign object damage (FOD), fatigue and thermal expansion mismatch due to thermal cycling, and thermochemical (corrosion) and thermomechanical (solid particle erosion) damage due to particle ingestion during engine operation.

Through several static laboratory studies, the thermochemical degradation of $Yb_2Si_2O_7$ by molten particles is well understood as a dissolution-reprecipitation mechanism. Across varying test temperatures, particle compositions, and loadings, $Yb_2Si_2O_7$ is readily dissolved by these particles primarily comprised of calcium magnesium aluminosilicates (CMAS), resulting in glass saturation and reprecipitation of $Yb_2Si_2O_7$ itself along with other extraneous phases [4–9]. Additionally, CMAS glass has been shown to infiltrate $Yb_2Si_2O_7$ via grain boundary transport, providing another pathway for melt ingress. These thermochemical and microstructural consequences of molten particle interactions will be exacerbated by other environmental factors in the engine. For example, water vapor can result in porosity/void formation as well as reduce melt viscosity leading to faster reaction, and thermal cycling will worsen thermal expansion mismatch and cyclic fatigue between extraneous phases and the coating. Finally, further mechanical (erosion/FOD) and corrosive damage can be initiated by successive ingestion of particles into the jet stream. Altogether, these damage mechanisms reduce the durability of the EBC system. It is crucial to understand the synergies of degradation to predict operating lifetimes of coatings and components. There is

a dearth of literature, however, in investigating $Yb_2Si_2O_7$ in an environment that incorporates these degradation modes simultaneously.

A few past studies on thermal barrier coating (TBC) damage by molten particles have highlighted the importance of combined degradation testing to capture engine environment failure modes. In the authors' own previous study [10], synergistic burner rig testing was carried out on a SOA 7 wt.% yttria stabilized zirconia (7YSZ) thermal barrier coating (TBC). While varying test temperature and particle size, the investigations were able to establish the interplay of erosion and corrosion by CMAS particles, as well as demonstrate the thermochemical degradation of 7YSZ previously observed on in-service components [11,12]. As observed on flight hardware, 7YSZ undergoes "progressive exfoliation" due to CMAS deposition along with thermal cycling of the engine [13]. The destabilization of the tetragonal structure along with CMAS solidification causes stress accumulation and stiffening, resulting in coating spallation. Consequently, a new unaffected layer of 7YSZ is exposed to further deposition, causing this process to repeat. These results contrasted with degradation previously reported in static furnace investigations of 7YSZ in which coatings were fully infiltrated by molten particles in minutes. Such differences in failure modes reinforce the need for laboratory scale testing that can replicate CMAS deposition observed on in-flight hardware. Given the immense expense and time required for full-scale engine testing, establishing the feasibility of burner rig testing for accurate assessment of materials durability, especially for SOA architectures, can aid in rapid evaluation of prospective materials, speeding up development of future coating systems. While the in-service degradation of $Yb_2Si_2O_7$ and other silicate-based EBCs have not been published in open literature, such evaluations will also be valuable in observing differences between different SOA materials in an applicable test environment.

The current study continues burner rig evaluation of SOA engine coatings with investigation of the particle-induced degradation of a $Yb_2Si_2O_7$ EBC system. In addition to characterizing interplay of erosion and corrosion in this system, it is also desired to carry out longer term corrosion testing of this EBC system to elucidate mechanisms of failure in a relevant testing environment, compared to previous static testing literature.

2. MATERIALS AND METHODS

A ~250 µm $Yb_2Si_2O_7$ topcoat was deposited via air plasma spray (APS) onto 25.4 mm diameter SiC Hexoloy substrates. A ~125 µm Si metal bondcoat was utilized to improve adhesion between the bondcoat and the substrate. All burner rig testing was carried out in NASA Glenn's Erosion Burner Rig Facility, which is Mach 0.3-1 Jet-A combustor modified to incorporate particle injection and deposition [14,15]. Particles were injected into the burner rig using a screw-driven particle feeder. Each sample was held with a clamshell fixture at the end of 305 mm unattached duct (19 mm in diameter). The samples were affixed 30 mm from the exit of the duct. A model four-component glass frit based on previously observed engine deposits [11] was synthesized with a nominal composition of 30.67CaO–8.25 MgO–12.81$AlO_{1.5}$–48.27SiO_2. The glass frit was sieved to three different particle sizes (~43 µm, ~86 µm, and ~168 µm) for testing. ~60 µm Al_2O_3 particles were also utilized in testing. As detailed in the authors' previous publication [10], calibration trials were carried out to set the particle loading rate as ~1 mg/cm^2 per deposition increment for each particle size (~2.8 mg per increment). This loading was chosen as being representative of a "fine" dust concentration, and what could be expected for an engine at standard cruise conditions. Images of the burner rig test set-up are shown in Figure 1.

These investigations were performed in three phases: Phase 1 evaluated the effect of particle size, test temperature, and deposition rate on the erosion/corrosion degradation of $Yb_2Si_2O_7$. These experiments mirror testing previously carried out on SOA 7YSZ and were performed to determine the crossover of erosion/corrosion for a $Yb_2Si_2O_7$ EBC system. Each glass frit particle size was deposited on the samples at three different flame temperatures: 650°C (below the glass transition temperature), 950°C (above the glass transition temperature), and 1300°C (above the melting temperature [~1240°C]). Additionally, as most standardized erosion testing is carried out using Al_2O_3 particles, the ~60 µm Al_2O_3 particles were also used in erosion testing at each temperature to determine how deposition rate affected mass change compared to literature values. ~60 µm Al_2O_3 particles were chosen for direct comparison to earlier erosion studies using this particle size.

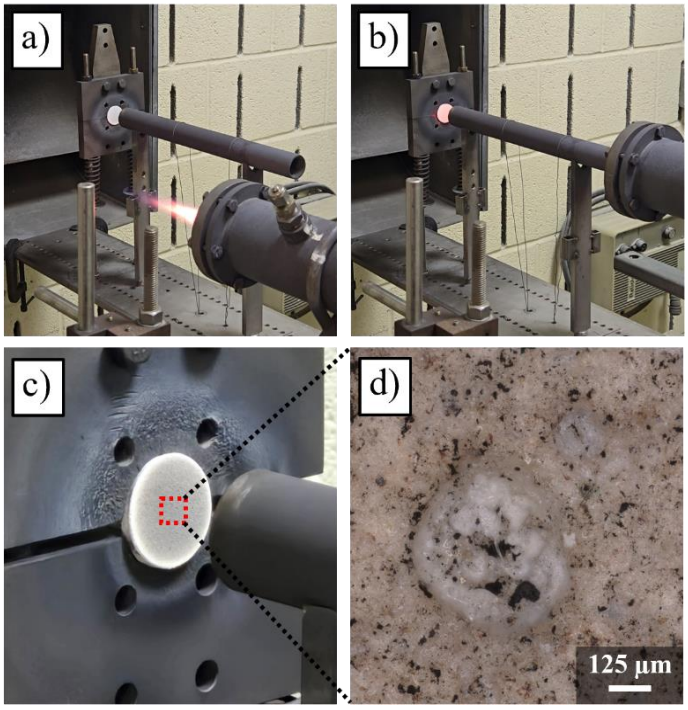

FIGURE 1. a) Burner rig torch in "off" position, b) Burner rig torch in "on" position, c) coating sample after testing and d) optical image of glassy deposits on the surface of the coating after testing.

The velocity of the particles at each temperature were measured using a double disk velocimeter [16]. For Phase 1, each sample was exposed to 10 increments of particle deposition, with mass measurements taken before and after each exposure to determine mass gain or loss.

Phase 2 was performed to determine the effects of thermal cycling on coating durability under CMAS deposition. To the best of the authors' knowledge, this is the first reported study on the evaluation of a $Yb_2Si_2O_7$ EBC system under CMAS degradation in a burner rig environment, and a SOA 7YSZ APS coating deposited on a CMSX-4 superalloy substrate was also tested under the same conditions. Testing in this phase was carried out utilizing the smallest glass frit particles (~43 µm) at 1300°C flame temperature. Each cycle consisted of 1 minute of hot time (torch on sample with CMAS deposition) and 1 minute of cold time (torch off sample with no CMAS deposition). After testing, optical images were acquired (Keyence VHX optical microscope) before the samples were cross sectioned, mounted in epoxy, and polished to a 1 µm finish. The cross sections were then imaged via back scattered (BSE) scanning electron microscopy (SEM) (Phenom ProX, Hitachi S4700).

Finally, Phase 3, provides an assessment of literature studies on CMAS testing of $Yb_2Si_2O_7$ along with the current set of analyses to compare dynamic to static results. The assessment is framed within previous estimations of proposed damage and engine failure for dust concentrations in flight.

3. RESULTS AND DISCUSSION

3.1. Phase 1: Effects of temperature, particle size, and deposition rate

Figure 2 displays the cumulative mass change plots of the coatings exposed to the CMAS glass frit. At both 650°C (Figure 2(a)) and 950°C (Figure 2(b)), mass loss was primarily observed for all particle sizes, indicating that the coatings were being eroded at these test conditions. The mass change curves at these temperatures exhibited a sharp drop in mass, followed by fairly linear mass loss. The high initial mass loss is characteristically attributed to the removal of surface asperities before reaching a steady state erosion rate. There was an overall decrease in magnitude of mass loss at 950°C compared to 650°C. 950°C is above the glass transition temperature of the glass frit, meaning that partially softened particles may not be as effective in eroding coatings as the particles used at 650°C, which are expected to be fully solid.

At 1300°C (Figure 2(c)), while exposures with both the 86 and 168 µm particles resulted in mass loss, exposure with 43 µm particles resulted in mass gain. The observed mass gain suggested adhesion of the CMAS particles to the coating. Additionally, the initial steep drop in mass loss for samples experiencing erosion was not observed at 1300°C. As previously mentioned, 1300°C is above the melting temperature of the glass frit. Thus, while the smaller particles were probably susceptible to complete melting (resulting in adhesion) while passing through the torch, larger particles may have only become partially molten, resulting in both adhesion and erosion occurring simultaneously and exhibiting an overall mass loss

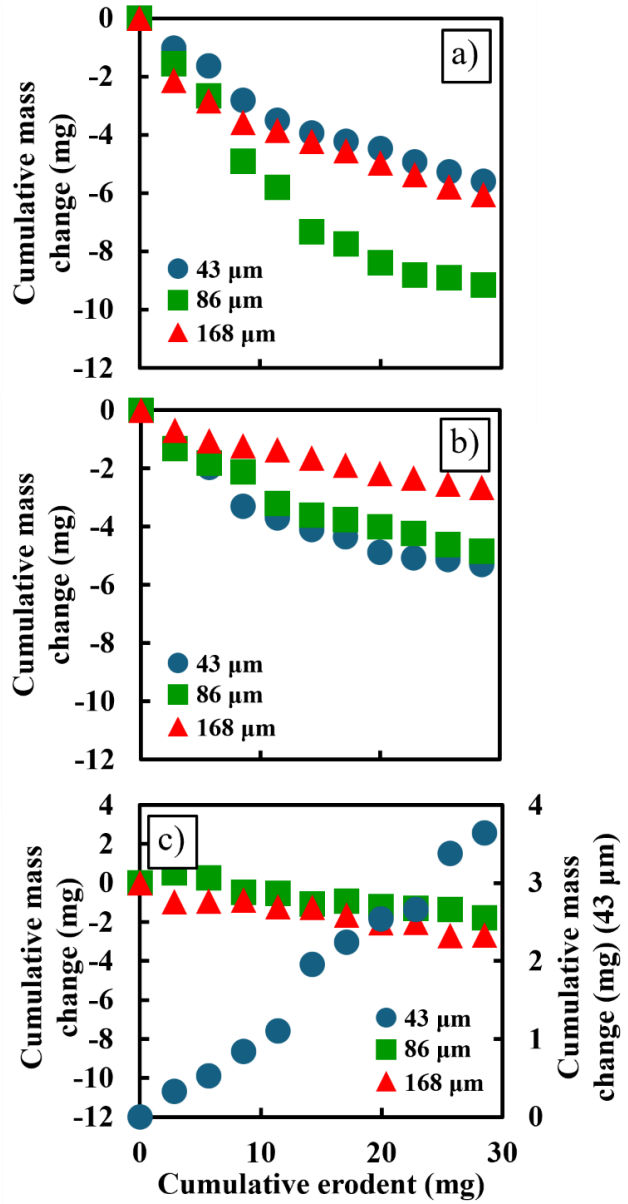

FIGURE 2. Cumulative mass change plots for CMAS deposition at a) 650°C, b) 950°C, and c) 1300°C. Note the secondary axis for the 43 µm sample in Figure 2(c).

response. Like results at 950°C, the overall magnitude of mass loss for the erosion-dominated samples at 1300°C was lower with increasing temperature, although mass loss did not trend with particle size.

Al_2O_3 particles are typically used in erosion testing of coating materials [17–20], so was important to use Al_2O_3 under similar conditions to determine the effects of particle chemistry and deposition rate. Figure 3 shows the mass change curves of two samples tested with 60 µm Al_2O_3 particles at 650°C and 1300°C (the lowest and highest flame temperatures in this study). Exposures at both temperatures resulted in erosion behavior, as indicated by the consistent mass loss. Interestingly at 1300°C, there was little to no change in mass observed at the

beginning of the test before exhibiting a sharp decrease in mass loss followed by steady state behavior, indicating that flame temperature also influenced erosion for Al_2O_3 particles as well. Like the mass change exhibited with CMAS particles, the magnitude of mass loss was lower at 1300°C than at 650°C.

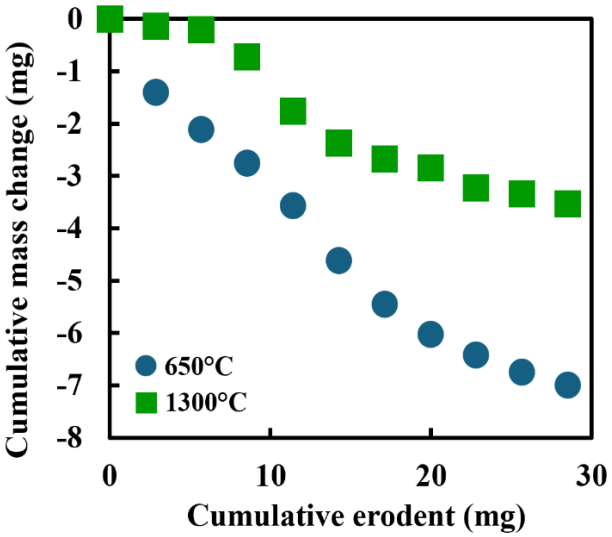

FIGURE 3. Cumulative mass change plots for 60 µm Al_2O_3 deposition at 650°C and 1300°C.

Although an influence of temperature was observed in the mass loss plots with both the CMAS frit and Al_2O_3 particles, mass loss did not trend with particle size. For example, at 650°C (Figure 2(a)), the sample eroded with 86 µm particles exhibited the greatest mass loss, while the mass losses for the samples eroded with the 43 µm and 168 µm particles were roughly equal. The steady-state erosion rate E is calculated by taking the slope of the linear region of the erosion curves (usually the last five points) as

$$E\left(\frac{mg}{g}\right) = \frac{\Delta m_s}{\Delta m_e} \quad (1)$$

where m_e is the mass of erodent and m_s is the mass of the sample. However, it is not possible to directly compare the rate calculated from Eq. 1 due to variations in particle size, which will affect the number of particle impacts at the surface of the coatings even when the total erodent mass per increment remains equal (i.e. more particle impacts for smaller particles vs larger particles for the same mass of erodent). Instead, the erosion rate can be calculated as mass loss per particle impact by multiplying by the mass of an individual particle (utilizing the density of the particles and approximating as spheres) [21,22]. For brittle materials, the erosion rate has shown to be related to particle kinetic energy U utilizing a power-law dependence

$$E\left(\frac{mg}{impact}\right) = \gamma U^b \quad (2)$$

where b is the kinetic energy exponent and γ is a proportionality constant that is a function of erosion test conditions [17,23–25]. Utilizing this relationship in Eq. 2, it is then possible to directly compare erosion rates between different particle sizes.

The relationship between particle kinetic energy and erosion rate is plotted in Figure 4. The regression fits for the kinetic energy model are displayed with dashed lines. The YbDS sample tested with the 43 µm particles at 1300°C was not included in this plot since mass gain and CMAS accumulation was primarily observed. At both 650°C and 950°C, the erosion data agrees well with the kinetic energy model, suggesting that YbDS undergoes brittle erosion during particle impingement. For comparison to previous testing in literature, data points from *Presby et al.* from the erosion of APS YbDS coatings using Al_2O_3 are also plotted [26]. As shown in the figure, this earlier data also follows the kinetic energy model, with a slope of b=1.22 calculated from regression analysis. The slopes for the CMAS eroded samples at 650°C and 950°C were b=1.24 and b=1.18, respectively. This suggests a similar mechanism of erosion between the particle chemistries, demonstrating that when CMAS particles maintain their hardness and are not fully molten, the CMAS acts as an effective erodent.

However, the Al_2O_3 erosion data on APS YbDS previously acquired by *Presby et al.* is roughly an order of magnitude lower than the erosion rates estimated in this study These results are akin to the authors previous study on the erosion of 7YSZ [10], where an effect of deposition rate on erosion rate was conjectured. It is important to note that the tests conducted by *Presby et al.* utilizing Al_2O_3 were carried out at a deposition rate of ~2 g/min, whereas both the CMAS and Al_2O_3 particles in this study were deposited at a maximum of ~0.0068 g/min. At higher deposition rates, it was hypothesized that the lower erosion rates were primarily caused by particle shielding, meaning that some incoming Al_2O_3 particles were interacting with rebounding particles, and therefore, not all particles contributed equally to the erosion process. While particle deposition and erosion are

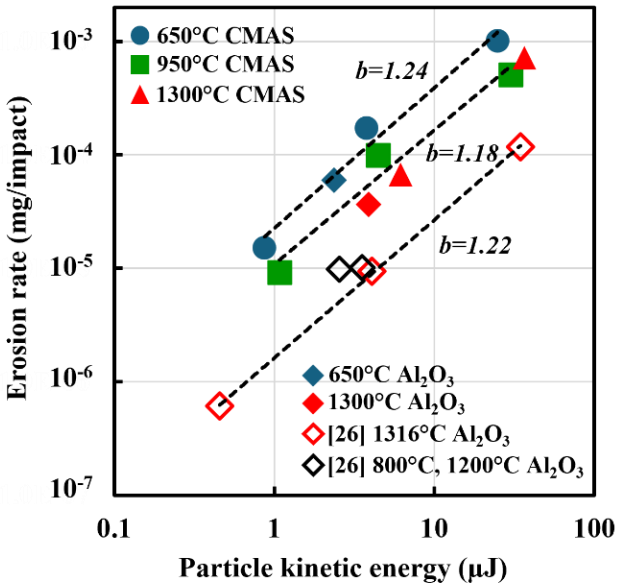

FIGURE 4. Steady-state erosion rate versus particle kinetic energy for APS YbDS.

both very complex phenomena, the current results do highlight the influence of particle flux on erosion rate and should be considered when evaluating coating materials. High particle fluxes are typically utilized in erosion testing, as they produce scars that are resemble damage seen from flight components over a shorter test period [27]. However, lower particle fluxes can be more relevant to engines in normal cruise conditions and may be more instructive in estimating true mass loss rates over time.

There was a slight dependence on temperature in the CMAS data, with erosion rates overall being lower with increasing temperature. As mentioned earlier, the CMAS particles were expected to become softened or even molten at higher temperatures, which would reduce the effectiveness of eroding the samples. A dependence on temperature can also be observed by looking at the erosion data acquired in this study utilizing the 60 µm Al_2O_3 particles. At 650°C, the erosion rate was 5.96×10^{-5} mg/impact and 3.65×10^{-5} mg/impact at 1300°C. Conversely, there was little to no effect of temperature observed in the *Presby et al.* data, which includes exposures done at 800°C, 1200°C, and 1316°C. Based on the *Presby et al.* data, it was presumed that erosion tests conducted with Al_2O_3 particles were less sensitive to temperature, given that Al_2O_3 melts at a much higher temperature (~2100°C) and changes in particle state (i.e. softened/molten) were not expected. It is important to note, however, that material mechanical properties can change as a function of temperature, including hardness, which is an important property in the estimation of volume loss in brittle materials due to particle impacts[28,29]. The hardness of sapphire (single crystal Al_2O_3) is ~20 GPa at room temperature, although its hardness has been measured to be ~5 GPa at 1000°C [30]. Additionally, across multiple grain sizes, the strength of Al_2O_3 has been shown to decrease between 30-60% from 800°C to 1500°C [31]. Overall, the possible decrease in mechanical durability of Al_2O_3 at increased temperatures may reduce the effectiveness of Al_2O_3 as an erodent. Based on current results, this effect may be more pronounced at lower particle deposition rates where individual impacts on coating surfaces are more probable over interactions with other particles. Thus, long-term flight relevant erosion phenomena may require extended testing at low particle fluxes to elucidate how coatings degrade over a service lifetime.

3.2. Phase 2: Effects of CMAS cyclic deposition on coating degradation

The degradation of 7YSZ by CMAS degradation on flight hardware is well documented in literature, and it was desired to carry out analyses to determine if YbDS as an EBC material underwent the same dramatic failure mechanism under similar test conditions. By utilizing a burner rig test setup, the effects of dynamic particle deposition, thermal cycling as well as the effect of a thermal gradient can be assessed. Initially in Phase 2, a 7YSZ sample and a YbDS sample were cycled for a total of 20 minutes, resulting in 10 total minutes of hot time (and equal to the amount of CMAS deposited in the 10 increments for the 43 µm particles during Phase 1). Optically, large portions of the 7YSZ coating (Figure 5(a)) spalled off after deposition, whereas the YbDS sample remained intact and no large changes in the coating were readily observed (Figure 5(b)). An additional YbDS sample was then cycled for 40 minutes (Figure 5(c)) (20 total minutes of hot time), and the largest change observed was the presence of a distinct CMAS layer adhered to the surface with no variation in coating microstructure.

Micrographs of an additional region of the corroded 7SYZ coating are displayed in Figure 6. In Figure 6(a), the micrograph of the full thickness of the remaining 7YSZ coating displays propagation of horizontal cracking, as well as regions of molten deposits remaining at the surface of the coating. The higher magnification micrograph of Figure 6(a) is shown in Figure 6(b), in which additional cracks were observed at the surface where several pockets of residual CMAS were observed. Particularly, CMAS films were also observed between the lamellar splats in this region. Finally, with higher magnification (Figure 6(c)), in addition to CMAS infiltration between the lamellar splats, the

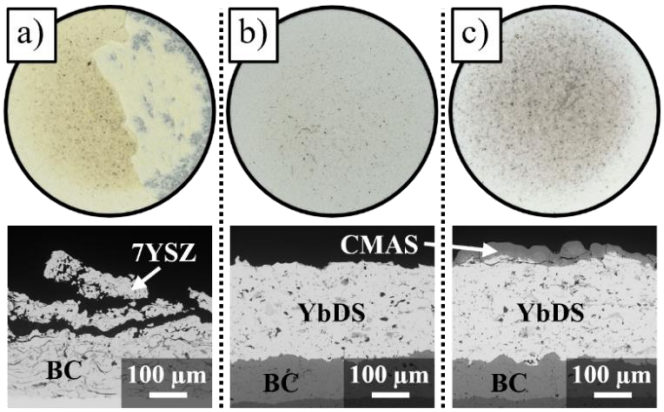

FIGURE 5. Optical and SEM images of a) APS 7YSZ coating exposed to 43 µm CMAS cyclic deposition at 1300°C for 20 minutes, b) APS YbDS coating exposed to 43 µm CMAS cyclic deposition at 1300°C for 20 minutes, and c) APS YbDS coating exposed to 43 µm CMAS cyclic deposition at 1300°C for 40 minutes.

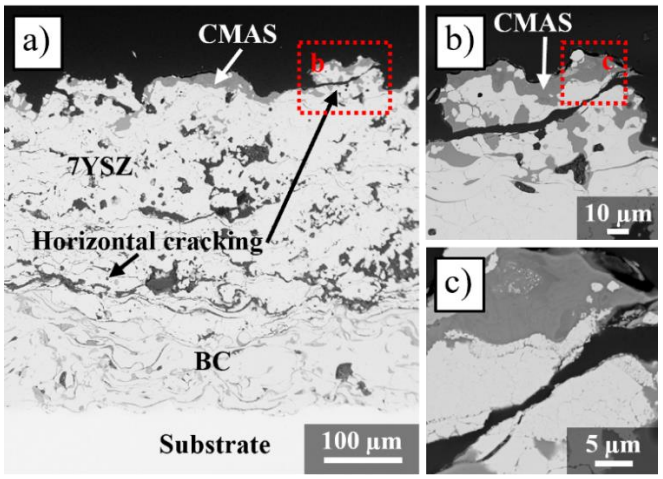

FIGURE 6. Higher magnification micrographs of the APS 7YSZ coating exposed to 43 µm CMAS cyclic deposition at 1300°C for 20 minutes.

presence of globular precipitates as well as CMAS films between grain boundaries indicate dissolution and precipitation occurring in the sample. While there was evidence of CMAS presence at the remaining surface of the coating, there was no evidence of CMAS infiltration deeper into the coating thickness. Along with the widespread spallation of the 7YSZ coating shown in Figure 5(a), this result correlates with previous observations of peeling layers of 7YSZ as it is exposed to CMAS deposits at high temperature [13]. Once cooled, the stresses due to phase transformation result in gradual delamination and fresh layers of coating to be exposed for further degradation. Unlike 7YSZ, cyclic exposure of YbDS for 20 minutes (10 minutes hot time) did not result in wide-spread coating spallation. Instead, a thin layer of CMAS deposit was observed at the surface, with little to no evidence of interaction or infiltration after deposition. As more CMAS was deposited, a continuous bumpy layer of molten silicate built up on the surface of the YbDS coating, as shown in Figure 5(c). Figure 7 displays higher magnification images of the

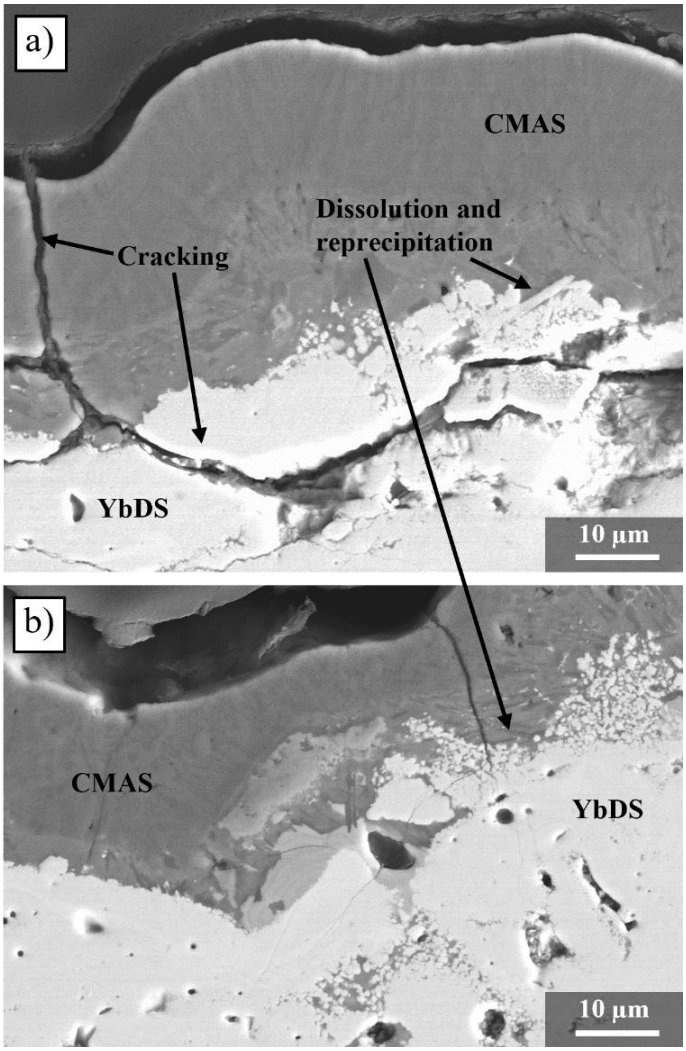

FIGURE 7. Higher magnification micrographs of the APS YbDS coating exposed to 43 µm CMAS cyclic deposition at 1300°C for 20 minutes.

the YbDS coating cycled with CMAS deposition for 40 minutes (20 minutes of hot time). This layer was ~50 µm thick at its highest point in some areas. Large cracks formed within the CMAS layer (Figure 7(a)), extending partially into the region of coating in contact with the molten deposit. Phase contrast in the BSE micrograph indicated some crystallization of the CMAS itself upon cooling, as evidenced by dendritic-like structures present in the image. These large cracks are possibly the result of stresses due to the thermal expansion mismatch between the CMAS deposit (~8-10×10^{-6}/K) [32,33] and YbDS (~4-4.5×10^{-6}/K) [34–36]. The crystallization of the CMAS upon cooling could also lead to volumetric expansion/contraction, leading to stress accumulation as well. Needle-like (Figure 7(a)) as well as smaller precipitates (Figure 7(b)) were also observed at the surface, suggesting that dissolution of the YbDS coating and reprecipitation of phases were also occurring after deposition. The needle-like precipitates are silicate apatite phases that commonly form in interactions of YbDS with molten silicates, whereas YbDS typically reprecipitates as equiaxed grains at equilibrium. Still, this corrosion was primarily limited to the surface and only extended ~10 µm into the coating.

Because little damage was observed in the YbDS samples with the shorter CMAS exposures, additional YbDS samples were tested for 2 hours (1 hour of hot time) and 4 hours (2 hours of hot time). A micrograph of the YbDS sample tested for 2 hours is displayed in Figure 8(a), in which a discontinuous layer of CMAS was observed at the surface of the coating. Energy dispersive spectroscopy (EDS) was utilized to determine the presence of CMAS in the sample (using calcium (Ca) as the identifying element). The map presented in Figure 8(b) indicated that CMAS was only present in deposits at the surface, with no traces of Ca within the depth of the coating. A higher magnification image of the interface between the deposit and the coating is displayed in Figure 8(c). Like the shorter exposures, precipitates observed in the residual CMAS suggested dissolution and reaction occurring between the glassy deposit and the coating, but no substantial degradation was present. Even the sample tested for a total of 4 hours (shown in Figure 8(d)) did not exhibit immense degradation, with residual CMAS also observed at the surface of the coating along with several traverse and vertical cracks. The cracks are consistent with cracking within the CMAS layer observed at 40 minutes of testing time, correlating with conjecture of thermal expansion mismatch between the glass and the coating from thermal cycling. However, the residual glassy deposits observed at both 2 hours and 4 hours of testing did not appear as a consistent layer across the surface of the coating, as observed in the sample cycled for 40 minutes (Figure 5(c)). With additional cycles, the cracks due to thermal cycling may have propagated, causing regions of the previously deposited CMAS to spall off. Hence, large globules of CMAS built up along the surface, as shown in Figure 8(d), were observed next to much thinner regions of glass.

3.3. Phase 3: Comparisons to static testing and damage regimes for flight hardware

It was interesting that limited degradation of the YbDS

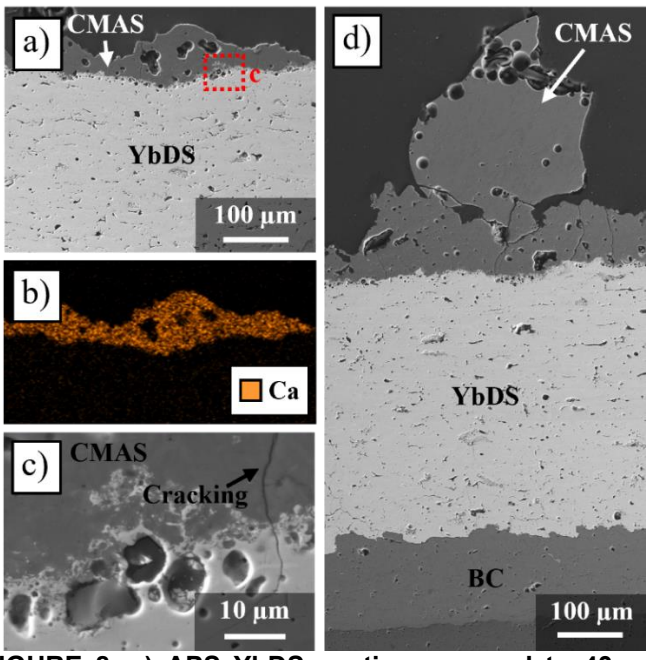

FIGURE 8. a) APS YbDS coating exposed to 43 µm CMAS cyclic deposition at 1300°C for 2 hours, b) EDS map of Figure 8(a), c) higher magnification image of Figure 8(a), and d) APS YbDS coating exposed to 43 µm CMAS cyclic deposition at 1300°C for 4 hours.

coating from CMAS deposition in this study was observed, given that several static testing studies at both short (minutes) and long exposure (100s of hours) times resulted in immense infiltration and reaction. YbDS does not undergo deleterious phase transformations as a function of temperature like 7YSZ, nor experiences any destabilization due to leaching of cations, although the propensity of reaction of disilicates with CMAS has been shown to depend on deposit chemistry and disilicate cation size [37,38]. Smaller cation disilicates tend to exhibit limited interaction with CMAS, and instead, degradation proceeds by infiltration via grain boundaries. In cases of dissolution, excess SiO_2 from the reactions can drive further infiltration. Although several CMAS studies have been conducted on bulk YbDS samples, very few have investigated the degradation of APS YbDS microstructures. The reaction pathway becomes more complex due to the presence of deposition morphology and defects, such as pores, unmelted particles, and phase inhomogeneity. The most relevant investigation to the current study was conducted by *Zhao et al.*, in which CMAS was applied at a loading of ~10 mg/cm^2 to plasma sprayed YbDS coatings and heat treated from 1 minute up to 200 hours to assess reactivity [5]. Selected micrographs from *Zhao et al.* are shown in Figure 9(a) and 9(d) along with the micrographs of the 2-hour (Figure 9(b)) and 4-hour (Figure 9(c)) cycled samples from this study to compare reaction extent. The red dashed line in each micrograph indicates reaction and interaction layer depth. The *Zhao et al.* static sample tested at 1300°C for 1 hour is displayed in Figure 9(a) and exhibited a ~25 µm thick reaction layer in the ~100 µm coating. Large-grained precipitates comprised this interaction region, along with cracks. Conversely, the 2-hour cycled (1 hour hot time) sample, exhibited limited reactivity with the CMAS deposits. The reaction layer was ~10 µm thick in the ~350 µm coating with very small precipitates present. For the 2-hour cycled sample, roughly 60 mg/cm^2 would have been injected from the burner to the sample. Though, even with a greater amount of CMAS deposited over time, substantially less infiltration was observed compared to the static sample. Similarly, with greater time and subsequent deposition, the 4-hour cycled samples exhibited roughly the same damage morphology as the 2-hour sample, albeit with greater layer thickness of residual CMAS deposits (as previously displayed in Figure 8). This contrasts with the static study in which greater exposure time (100 hours) with the same amount of CMAS resulted in further infiltration into the coating (Figure 9(d)).

Unlike static isothermal exposures, the samples tested in this study were only heated from one side, inadvertently driving a thermal gradient through the coating. While it is unknown the exact magnitude of that gradient, the viscosity and thus mobility of glasses decrease with decreasing temperature [39], meaning that some infiltration may have been halted simply by the lack of driving force of temperature. Additionally, as CMAS accumulated at the surface, these deposits could have acted as an insulating layer, reducing heat transfer through the sample. All these factors are expected to occur during engine operation, meaning that the speed at which reactions occur at relevant conditions may be lower than previously assumed based on isothermal results. It was originally planned to continue testing with the 4-hour sample; however, after several hours of being at 25°C and upon reheating in the burner rig, part of the coating did spall. Although not picture here, cross sectional SEM analysis of the region indicated that no CMAS had substantially infiltrated the coating before spallation. During cycling, the surfaces of the coatings cooled to ~500°C during burner "off" times. This suggests that failure of the coating was not due to CMAS reaction per say, but rather thermal shock after heating rapidly again from room temperature. Due to instrumentation limitations, it was not possible to conduct a continuous exposure beyond 4 hours, although it is desired to induce CMAS-driven failure in a YbDS-based coating system and compare to failures observed from static tests. Still, this vast difference in damage observed between burner rig and static investigations emphasizes how the amount of CMAS, application methods, and testing conditions affect degradation results. These results also stress the importance of framing CMAS testing results within various flight conditions that may occur on in-service components.

Borom et. al published one of the first studies to document particulate damage of TBCs from flight hardware [11]. In this paper, the authors theorized that short-term and long-term damage would greatly depend on surface temperature, exposure time, and "dirt load", as shown in a diagram in Figure 10(a), with investigations from aircraft operating in the Middle East as well as the southwestern United States as the basis for these observations. Equally, *Clarkson et al.* developed a duration of exposure versus ash concentration (DEvAC) chart (Figure 10(b))

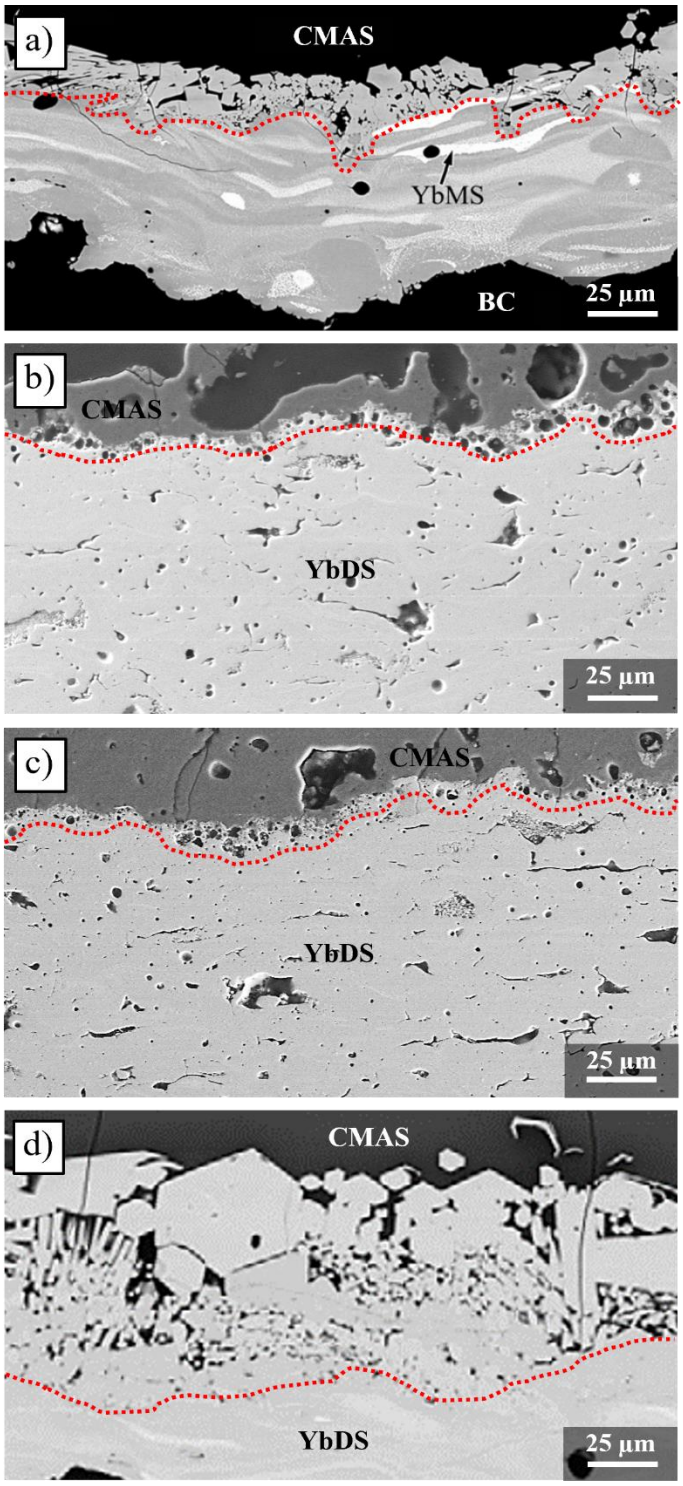

FIGURE 9. SEM images of a) *Zhao et al.* [5] static APS YbDS coating heat treated with 10 mg/cm^2 of CMAS at 1300°C for 1 hour, b) APS YbDS coating exposed to 43 µm CMAS cyclic deposition at 1300°C for 2 hours c) APS YbDS coating exposed to 43 µm CMAS cyclic deposition at 1300°C for 4 hours, and d) *Zhao et al.* static APS YbDS coating heat treated with 10 mg/cm^2 of CMAS at 1300°C for 100 hours.

from flight data across multiple technologies to determine engine susceptibility to particle damage [40,41]. To frame the current results within the failure regimes depicted by *Clarkson et al*. in Figure 10, an approximate ash concentration was estimated using combustion calculations of the burner rig set up. As discussed in the materials and methods section, the burner rig is a Jet-A combustor utilizing pre-heated, pressurized air as the oxidizer. Basic combustion analyses were carried out using the Chemical Equilibrium with Applications (CEA) program, developed by NASA [42]. Using this program, equilibrium combustion products and adiabatic flame temperature were determined. The

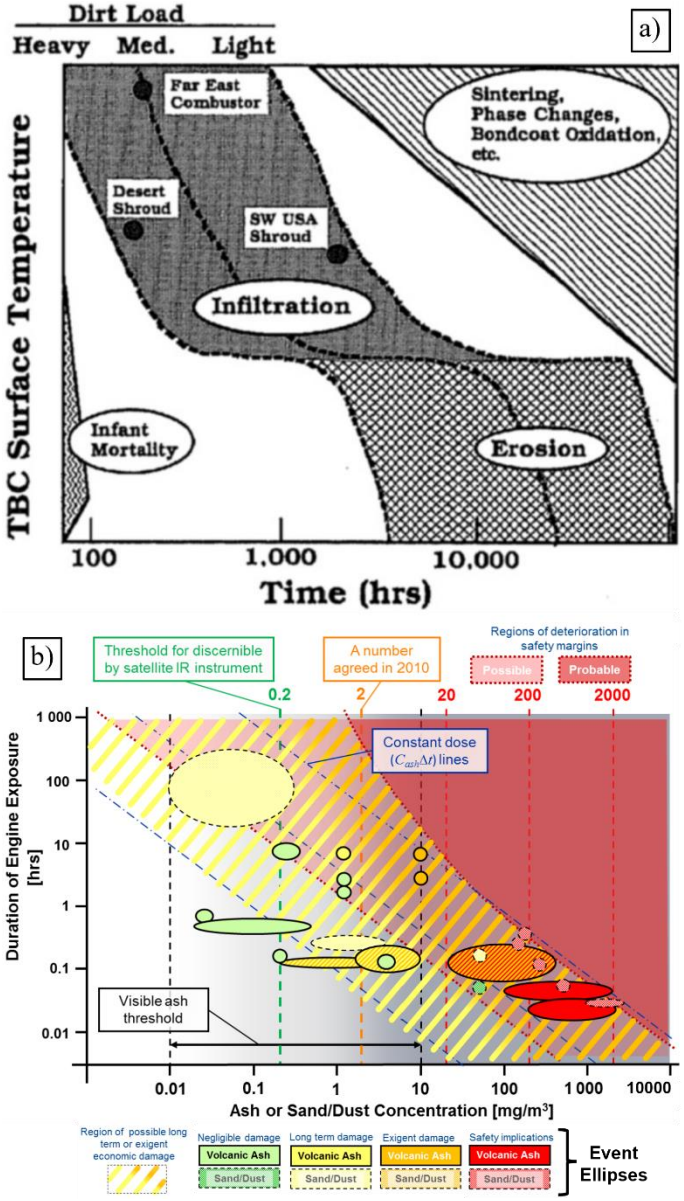

FIGURE 10. a) Hypothetical in-service failure regimes for APS 7YSZ TBCs from *Borom et al.* [11] and b) exigent and long-term damage regions for volcanic ash exposures in airplane engines from *Clarkson et al.* [40,41]

calculations were performed with the fuel entering the burner at 25°C, the pre-heated air at 205°C, and the burner pressure at 16.7 psi (1.14 atm).

The equivalence ratio (φ) is defined as

$$\varphi = \frac{(\dot{m}_f/\dot{m}_{ox})_a}{(\dot{m}_f/\dot{m}_{ox})_{st}} \quad (3)$$

where $\dot{m}_f$ and $\dot{m}_{ox}$ are the mass flow rates of the fuel and oxidizer, respectively, and "*a*" and "*st*" represent the actual and stoichiometric ratios of fuel to oxidizer. At 1300°C test conditions, the mass flow rate of the fuel was measured as 0.871 g/s and the mass flow rate of the air was 18.144 g/s. Taking the ratio of these values, the actual fuel to air ratio was 0.048. From CEA the stoichiometric ratio for Jet-A/air combustion, is 0.0681. Thus, the equivalence ratio was determined to be

$$\varphi = \frac{(\dot{m}_f/\dot{m}_{ox})_a}{(\dot{m}_f/\dot{m}_{ox})_{st}} = \frac{0.048}{0.068} \approx 0.70 \quad (4)$$

The combustion products and adiabatic flame temperature as a function of equivalence ratio are plotted in Figure 11, with the equivalence ratio of the 1300°C burner rig tests marked by the vertical dashed line. The adiabatic flame temperature (~1700°C) at the current test conditions was higher than the flame temperature measured by thermocouple, although this was somewhat expected given heat losses to the surrounding environment. Utilizing the equivalence ratio, it was then possible to estimate the Mach number and subsequent volumetric gas flow with combustion. The Mach number was calculated from a relationship for steady one-dimensional flow from an infinite reservoir from which gas is accelerated isentropically to its actual speed [43]. The Mach number *M* is expressed as

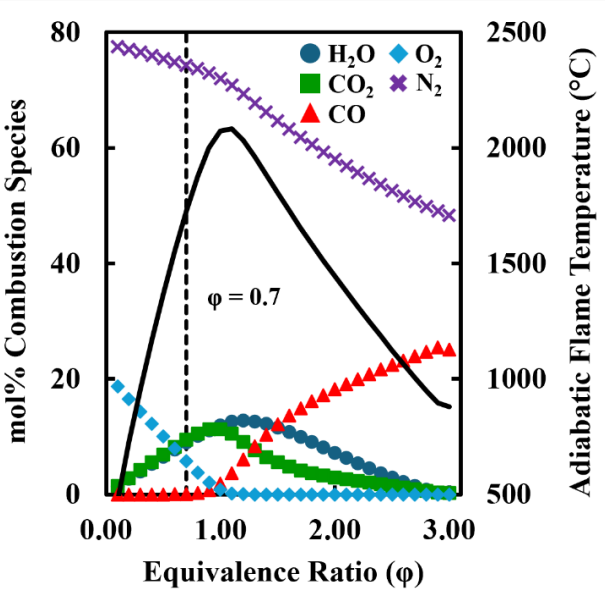

FIGURE 11. Combustion species concentration and adiabatic flame temperatures from CEA analysis as a function of equivalence ratio.

$$M = \sqrt{\left(\frac{2}{\gamma-1}\right)\left[\left(\frac{P_b}{p_e}\right)^{\frac{\gamma-1}{\gamma}} - 1\right]} \quad (5)$$

where $P_b/p_e = 1.14$ is the ratio of the back (combustion) pressure (16.7 psi) to the exit (atmosphere) pressure (14.7 psi) and $\gamma = 1.24$ is the ratio of specific heats obtained from CEA for an equivalence ratio of 0.7. The Mach number *M* was determined to be 0.46. The sonic velocity from CEA was 844.5 m/s, meaning that the velocity *V* of the gas was

$$V = M * 844.5 = 0.46 * 844.5 = 385.43\ m/s \quad (6)$$

Higher fidelity CFD modelling of the same combustor showed good agreement with the current set of analyses, with respect to gas velocity [15,44]. Therefore, while the current set of calculations are comparatively quite simple, the set of assumptions used for these estimations appear reasonable. Taking into consideration the diameter of the nozzle (0.019 m), the volumetric gas flow at the nozzle exit would be 0.11 m^3/s (the gas velocity times the cross-sectional area). Finally, the particle feed rate was ~3.6 mg/min, so the estimated particle concentration of the burner during testing was ~0.55 mg/m^3) (the particle feed rate divided by the volumetric gas flow).

Figure 12 displays a recreated DEvAC chart from *Clarkson et al.* depicting the calculated ash/dust concentration versus duration of engine exposure for the burner rig tests conducted in this study. The purple oval denotes the burner rig exposures conducted on YbDS, while the blue circles denote the exposures carried out on YSZ. In addition to the current study of exposures done at ~1 mg/cm^2, an additional data point was included from the author's previous study [10], in which YSZ was exposed to ~630 mg of CMAS over a 5 minute exposure (~25 $mg/cm^2/min$) under the same test conditions, resulting in an approximate ash/dust concentration of ~19 mg/m^3. At these test conditions, the coating experienced immediate catastrophic failure after testing, with >80% of the coating exhibiting immense spallation down to the substrate. The ash/dust concentrations calculated herein place the YbDS and low concentration YSZ exposures in the "long term damage" (yellow) region of the chart, which *Clarkson et al.* describes as "detectable abnormal deterioration in engine performance or reduction in the service life of one or more components". Although the YbDS coating itself did not display any microstructural damage on its own, the buildup of CMAS deposits over time could affect aerodynamic efficiency, or cause coating spallation due to thermal shock, as previously discussed. YSZ exhibited spallation and peeling during testing, which correlates to a reduction in service life of a particular component with that coating. Overall, the implication of "long-term damage" from this DEvAC chart agrees well with observations of coating behavior during burner rig testing. Similarly, *Clarkson et al.* described "exigent damage" (orange region of the chart) as the most problematic category of economic damage", meaning "engine damage that needs immediate attention (e.g. extensive cleaning or aircraft repair)

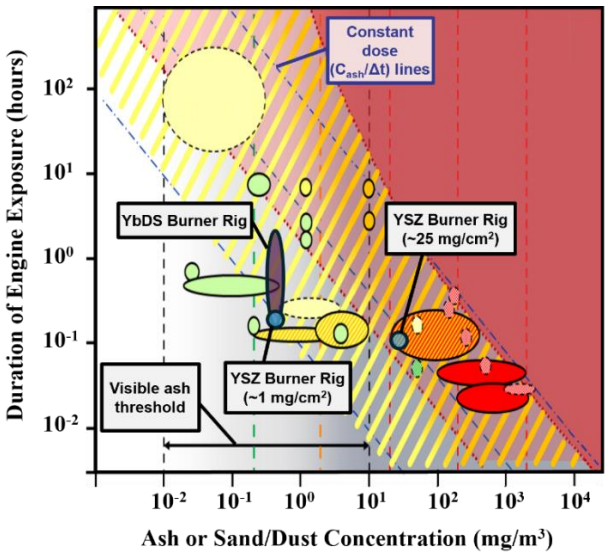

FIGURE 12. *Clarkson et al.* [40] DEvAC chart with APS YbDS and APS 7YSZ burner rig tests.

and potentially immediate removal of the engine from the aircraft." This explanation correlates well with observations of widespread catastrophic failure of YSZ at the higher ash/dust concentration. Though the *Borom* and *Clarkson* charts differ in particulate type (desert sand versus volcanic ash) in general, both diagrams indicate that a high concentration of dirt ingestion along with high surface temperatures will result in shorter operating lifetimes of protective coatings for engine components. While static tests do not necessarily capture the effects of gradual CMAS deposit build up over time, the total accumulation observed in testing by *Zhao et al.* is analogous to what could be expected for an engine experiencing "high" dirt load at very short times (~100s of hours according to the chart by *Borom et al.*). Meanwhile, the samples tested in the current study would be classified as "light" dirt load. Even though these samples were only cycled for a maximum of 4 hours, based on the current observations of limited interaction at a shorter time scale, their long-term damage would probably be akin to what was expected for sintering and phase changes, occurring thousands of hours into service.

Most static exposures are often representative of worst-case scenarios of high concentrations of dust ingestion. Lower deposition rates in dynamic exposures incorporating additional environmental damage mechanisms can aid in elucidating discrete differences in reactivity between materials and longer-term degradation pathways. In the current study, it was shown that 7YSZ undergoes immense spallation with high temperature particulate exposure at fine concentrations, whereas YbDS seemed to be more resistant than 7YSZ to degradation under the same set of conditions, demonstrating the usefulness of determining differences in reaction propensity between materials. Although it is important to note that with increased air traffic and expansion into markets in dustier regions of the world like Northern Africa or the Middle East, medium to heavier dirt loads may become an even greater issue at standard cruise conditions. Overall, this study demonstrates that more work is needed to fully understand the effects of CMAS deposition and test methodology on understanding coating durability and life.

Burner rig testing has been emphasized in this paper as an improvement over static testing methods, as additional damage mechanisms (thermal cycling, thermal gradient, dynamic particle deposition) can be introduced to a sample, leading to greater relevancy in testing. However, there are limitations to the use of atmospheric burner rigs. Because this specific burner rig was run at atmosphere, the influence of higher pressures as well as increased water vapor concentration (a key EBC and SiC-based CMC failure mechanism) could not be investigated. It would be prudent in future investigations to conduct such a study in a combustion rig in which all these damage mechanisms would be incorporated. However, burner rigs still offer valuable data as a test rig capable of introducing high temperature particle deposition to prospective coating materials and assessing differences in pertinent environments.

4. CONCLUSIONS

Environmental barrier coatings (EBCs) are integral to the continued use of SiC-based CMCs in next generation gas turbine engines. Their degradation by particle interactions, however, must be investigated to determine their operating lifetimes. In this study, a SOA ytterbium disilicate (YbDS) EBC was tested at various temperatures with varying particle sizes of glass frit and Al_2O_3 to determine the relationship between erosion and corrosion, as well as the effects of thermal cycling and gradient on damage propagation. Regarding erosion mechanisms, the influence of test temperature was exacerbated when testing with lower particle fluxes. On the corrosion of YbDS by molten deposits, YbDS does undergo dissolution and reprecipitation, albeit at much slower rates than previously expected from static exposures in literature. YbDS was more robust against particle corrosion compared to a SOA 7YSZ TBC, and the presented results were compared to hypothetical service regimes from flight components. The current set of analyses contributes to ongoing understanding on improving future coating systems against particle degradation and improving testing methods for accurate assessments of operating lifetime.

ACKNOWLEDGEMENTS

This work was supported under the Transformational Tools and Technologies (TTT) project and the Hybrid Thermally Efficient Core (HyTEC) project within NASA's Aeronautics Research Mission Directorate (ARMD).

REFERENCES

[1] Lee, K. N., 2014, "Environmental Barrier Coatings for SiCf/SiC," *Ceramic Matrix Composites: Materials, Modeling and Technology*, N.P. Bansal, and J. Lamon, eds., John Wiley and Sons, Inc., Hoboken, NJ, pp. 430–451. https://doi.org/10.1002/9781118832998.ch15.

[2] Costa, G. C. C., and Jacobson, N. S., 2015, "Mass Spectrometric Measurements of the Silica Activity in the Yb2O3-SiO2 System and Implications to Assess the

Degradation of Silicate-Based Coatings in Combustion Environments," J. Eur. Ceram. Soc., **35**(15), pp. 4259–4267. https://doi.org/10.1016/j.jeurceramsoc.2015.07.019.

[3] Lee, K. N., Fox, D. S., and Bansal, N. P., 2005, "Rare Earth Silicate Environmental Barrier Coatings for SiC/SiC Composites and Si3N4 Ceramics," J. Eur. Ceram. Soc., **25**(10), pp. 1705–1715. https://doi.org/10.1016/j.jeurceramsoc.2004.12.013.

[4] Wiesner, V. L., Scales, D., Johnson, N. S., Harder, B. J., Garg, A., and Bansal, N. P., 2020, "Calcium–Magnesium Aluminosilicate (CMAS) Interactions with Ytterbium Silicate Environmental Barrier Coating Material at Elevated Temperatures," Ceram. Int., **46**(10), pp. 16733–16742. https://doi.org/10.1016/j.ceramint.2020.03.249.

[5] Zhao, H., Richards, B. T., Levi, C. G., and Wadley, H. N. G., 2016, "Molten Silicate Reactions with Plasma Sprayed Ytterbium Silicate Coatings," Surf. Coat. Technol., **288**, pp. 151–162. https://doi.org/10.1016/j.surfcoat.2015.12.053.

[6] Stokes, J. L., Harder, B. J., Wiesner, V. L., and Wolfe, D. E., 2019, "High-Temperature Thermochemical Interactions of Molten Silicates with Yb2Si2O7 and Y2Si2O7 Environmental Barrier Coating Materials," J. Eur. Ceram. Soc., **39**(15), pp. 5059–5067. https://doi.org/10.1016/j.jeurceramsoc.2019.06.051.

[7] Wiesner, V. L., Harder, B. J., Garg, A., and Bansal, N. P., 2020, "Molten Calcium–Magnesium–Aluminosilicate Interactions with Ytterbium Disilicate Environmental Barrier Coating," J. Mater. Res., **35**(17), pp. 2346–2357. https://doi.org/10.1557/jmr.2020.211.

[8] Turcer, L. R., Krause, A. R., Garces, H. F., Zhang, L., and Padture, N. P., 2018, "Environmental-Barrier Coating Ceramics for Resistance against Attack by Molten Calcia-Magnesia-Aluminosilicate (CMAS) Glass: Part II, β-Yb2Si2O7 and β-Sc2Si2O7," J. Eur. Ceram. Soc., **38**(11), pp. 3914–3924. https://doi.org/10.1016/j.jeurceramsoc.2018.03.010.

[9] Wolf, M., Mack, D. E., Guillon, O., and Vaßen, R., 2020, "Resistance of Pure and Mixed Rare Earth Silicates against Calcium-magnesium-aluminosilicate (CMAS): A Comparative Study," Journal of the American Ceramic Society, **103**(12), pp. 7056–7071. https://doi.org/10.1111/jace.17328.

[10] Stokes, J. L., and Presby, M. J., 2024, "A Dynamic Testing Approach for Particulate Erosion–Corrosion for Gas Turbine Coatings," J. Eng. Gas Turbine. Power, **146**(11), pp. 1–8. https://doi.org/10.1115/1.4065886.

[11] Borom, M. P., Johnson, C. A., and Peluso, L. A., 1996, "Role of Environmental Deposits and Operating Surface Temperature in Spallation of Air Plasma Sprayed Thermal Barrier Coatings," Surf. Coat. Technol., **86–87**, pp. 116–126.

[12] Smialek, J. L., 1991, "The Chemistry of Saudi Arabian Sand - A Deposition Problem on Helicopter Turbine Airfoils," NASA/TM.

[13] Mack, D. E., Wobst, T., Jarligo, M. O. D., Sebold, D., and Vaßen, R., 2017, "Lifetime and Failure Modes of Plasma Sprayed Thermal Barrier Coatings in Thermal Gradient Rig Tests with Simultaneous CMAS Injection," Surf. Coat. Technol., **324**, pp. 36–47. https://doi.org/10.1016/j.surfcoat.2017.04.071.

[14] Fox, D. S., Miller, R. A., Zhu, D., Perez, M., Cuy, M. D., and Robinson, R. C., 2011, "Mach 0.3 Burner Rig Facility at the NASA Glenn Materials Research Laboratory," NASA/TM--2011-216986 https://ntrs.nasa.gov/archive/nasa/casi.ntrs.nasa.gov/20110008403.pdf. [Online]. Available: https://ntrs.nasa.gov/archive/nasa/casi.ntrs.nasa.gov/20110008403.pdf. [Accessed: 11-Apr-2018].

[15] Miller, R. A., and Kuczmarski, M. A., 2013, "Burner Rig for Small Particle Erosion Testing of Thermal Barrier Coatings," J. Test. Eval., **42**(3). https://doi.org/10.1520/JTE20120303.

[16] Presby, M. J., 2021, "High-Temperature Solid Particle Erosion in a Melt-Infiltrated SiC/SiC Ceramic Matrix Composite," J. Eng. Gas Turbine. Power, **143**(12), pp. 1–6. https://doi.org/10.1115/1.4051969.

[17] Shin, D., and Hamed, A., 2018, "Influence of Micro–Structure on Erosion Resistance of Plasma Sprayed 7YSZ Thermal Barrier Coating under Gas Turbine Operating Conditions," Wear, **396–397**, pp. 34–47. https://doi.org/10.1016/j.wear.2017.11.005.

[18] Nicholls, J. R., Deakin, M. J., and Rickerby, D. S., 1999, "A Comparison between the Erosion Behaviour of Thermal Spray and Electron Beam Physical Vapour Deposition Thermal Barrier Coatings," Wear, **233–235**, pp. 352–361. https://doi.org/10.1016/S0043-1648(99)00214-8.

[19] Presby, M. J., Stokes, J. L., and Harder, B. J., 2024, "Solid Particle Erosion in Ceramic Matrix Composites and Environmental Barrier Coatings: A Perspective," Journal of the American Ceramic Society, **107**(3), pp. 1776–1792. https://doi.org/10.1111/jace.19376.

[20] Schmitt, M. P., Harder, B. J., and Wolfe, D. E., 2016, "Process-Structure-Property Relations for the Erosion Durability of Plasma Spray-Physical Vapor Deposition (PS-PVD) Thermal Barrier Coatings," Surf. Coat. Technol., **297**, pp. 11–18. https://doi.org/10.1016/j.surfcoat.2016.04.029.

[21] Ritter, J. E., 1992, "Particle Impact Damage of Engineering Ceramics," *Fracture Mechanics of Ceramics*, R.C. Brandt, ed., New York, pp. 555–578.

[22] Wiederhorn, S. M., and Hockey, B. J., 1983, "Effect of Material Parameters on the Erosion Resistance of Brittle Materials," J. Mater. Sci., **18**(3), pp. 766–780. https://doi.org/10.1007/BF00745575.

[23] Cernuschi, F., Guardamagna, C., Capelli, S., Lorenzoni, L., Mack, D. E., and Moscatelli, A., 2016, "Solid Particle Erosion of Standard and Advanced Thermal Barrier Coatings," Wear, **348–349**, pp. 43–51. https://doi.org/10.1016/j.wear.2015.10.021.

[24] Cernuschi, F., Lorenzoni, L., Capelli, S., Guardamagna, C., Karger, M., Vaßen, R., von Niessen, K., Markocsan, N., Menuey, J., and Giolli, C., 2011, "Solid Particle Erosion of Thermal Spray and Physical Vapour Deposition Thermal Barrier Coatings," Wear, **271**(11–12), pp. 2909–2918. https://doi.org/10.1016/j.wear.2011.06.013.

[25] Singh, S., Singh, D., Singh, J. P., Singh, R. N., and Routbort, J. L., 2005, "Solid-Particle Erosion of Thin Films Deposited on Ceramics," *Advances in Ceramic Coatings and Ceramic-Metal Systems: Ceramic Engineering and Science Proceedings, Volume 26*, pp. 190–198. https://doi.org/10.1002/9780470291238.ch23.

[26] Presby, M. J., Stokes, J. L., Harder, B. J., Lee, K. N., and Hoffman, L. C., 2023, "High-Temperature Solid Particle Erosion of Environmental and Thermal Barrier Coatings," Coatings, **13**(5), p. 902. https://doi.org/10.3390/coatings13050902.

[27] Bruce, R. W., 1998, "Development of 1232°C (2250°F) Erosion and Impact Tests for Thermal Barrier Coatings," Tribology Transactions, **41**(4), pp. 399–410. https://doi.org/10.1080/10402009808983765.

[28] Aquaro, D., and Fontani, E., 2001, "Erosion of Ductile and Brittle Materials (Development of a FEM-Based Model and Its Assessment Against Theoretical Models and Experimental Data)," Meccanica, **36**, pp. 651–661. [Online]. Available: https://link-springer-com.ezaccess.libraries.psu.edu/content/pdf/10.1023%2FA%3A1016396719711.pdf. [Accessed: 09-May-2018].

[29] Marshall, D. B., Lawn, B. R., and Evans, A. G., 1982, "Elastic/Plastic Indentation Damage in Ceramics: The Lateral Crack System," Journal of the American Ceramic Society, **65**(11), pp. 561–566. https://doi.org/10.1111/j.1151-2916.1982.tb10782.x.

[30] Alpert, C. P., Chan, H. M., Bennison, S. J., and Lawn, B., 1988, "Temperature Dependence of Hardness of Alumina-Based Ceramics," Journal of the American Ceramic Society, **71**(8), p. C-371-C-373. https://doi.org/10.1111/j.1151-2916.1988.tb06394.x.

[31] Spriggs, R. M., Mitchell, J. B., and Vasilos, T., 1964, "Mechanical Properties of Pure, Dense Aluminum Oxide as a Function of Temperature and Grain Size," Journal of the American Ceramic Society, **47**(7), pp. 323–327. https://doi.org/10.1111/j.1151-2916.1964.tb12994.x.

[32] Luckhardt, C. A., and Opila, E. J., 2025, "Experimental Investigation of Fifth Oxide Effects on Calcium–Magnesium–Aluminosilicate Glass Properties," Int. J. Appl. Glass Sci., **16**(4). https://doi.org/10.1111/ijag.70003.

[33] Wiesner, V. L., and Bansal, N. P., 2015, "Mechanical and Thermal Properties of Calcium–Magnesium Aluminosilicate (CMAS) Glass," J. Eur. Ceram. Soc., **35**(10), pp. 2907–2914. https://doi.org/10.1016/j.jeurceramsoc.2015.03.032.

[34] Fernández-Carrión, A. J., Allix, M., and Becerro, A. I., 2013, "Thermal Expansion of Rare-Earth Pyrosilicates," Journal of the American Ceramic Society, **96**(7), pp. 2298–2305. https://doi.org/10.1111/jace.12388.

[35] Stokes, J. L., Harder, B. J., Wiesner, V. L., and Wolfe, D. E., 2022, "Crystal Structures and Thermal Expansion of Yb2Si2O7–Gd2Si2O7 Solid Solutions," J. Solid State Chem., **312**(March), p. 123166. https://doi.org/10.1016/j.jssc.2022.123166.

[36] Ueno, S., Jayaseelan, D. D., Kita, H., Ohji, T., and Lin, H. T., 2006, "Comparison of Water Vapor Corrosion Behaviors of $Ln_2Si_2O_7$ (Ln=Yb and Lu) and $ASiO_4$ (A=Ti, Zr and Hf) EBC's," Key Eng. Mater., **317–318**, pp. 557–560. https://doi.org/10.4028/www.scientific.net/KEM.317-318.557.

[37] Summers, W. D., Poerschke, D. L., Park, D., Shaw, J. H., Zok, F. W., and Levi, C. G., 2018, "Roles of Composition and Temperature in Silicate Deposit-Induced Recession of Yttrium Disilicate," Acta Mater., **160**, pp. 34–46. https://doi.org/10.1016/j.actamat.2018.08.043.

[38] Stokes, J. L., Harder, B. J., Wiesner, V. L., and Wolfe, D. E., 2020, "Effects of Crystal Structure and Cation Size on Molten Silicate Reactivity with Environmental Barrier Coating Materials," Journal of the American Ceramic Society, **103**(1), pp. 622–634. https://doi.org/10.1111/jace.16694.

[39] Wiesner, V. L., Vempati, U. K., and Bansal, N. P., 2016, "High Temperature Viscosity of Calcium-Magnesium-Aluminosilicate Glass from Synthetic Sand," Scr. Mater., **124**, pp. 189–192. https://doi.org/10.1016/j.scriptamat.2016.07.020.

[40] Clarkson, R., and Simpson, H., 2017, "Maximising Airspace Use During Volcanic Eruptions: Matching Engine Durability against Ash Cloud Occurrence. Specialists' Meeting on Impact of Volcanic Ash Clouds on Military Operations, Conference: NATO STO-MP-AVT-272-20, May," *NATO STO AVT-272*.

[41] Clarkson, R. J., Majewicz, E. J. E., and Mack, P., 2016, "A Re-Evaluation of the 2010 Quantitative Understanding of the Effects Volcanic Ash Has on Gas Turbine Engines," Proc. Inst. Mech. Eng. G J. Aerosp. Eng., **230**(12), pp. 2274–2291. https://doi.org/10.1177/0954410015623372.

[42] McBride, B. J., and Gordon, S., 1996, *Computer Program for Calculation of Complex Chemical Equilibrium Compositions and Applications II. Users Manual and Program Description - 2*, Cleveland.

[43] Zucrow, M. J., and Hoffman, J. D., 1976, *Gas Dynamics*, Wiley.

[44] Kuczmarski, M. A., Miller, R. A., and Zhu, D., 2011, "CFD-Guided Development of Test Rigs for Studying Erosion and Large-Particle Damage of Thermal Barrier Coatings," Modelling and Simulation in Engineering, **2011**. https://doi.org/10.1155/2011/837921.